Available online at www.sciencedirect.com

ScienceDirect

Journal of Magnesium and Alloys 12 (2024) 1496–1510

www.elsevier.com/locate/jma

Full Length Article

Comparative analysis of microstructure, mechanical, and corrosion properties of biodegradable Mg-3Y alloy prepared by selective laser melting and spark plasma sintering

P. Minárik[a,b,*], M. Zemková[a], S. Šašek[a], J. Dittrich[a], M. Knapek[a], F. Lukáč[a,c], D. Koutný[d], J. Jaroš[d], R. Král[a]

[a] Faculty of Mathematics and Physics, Charles University, Ke Karlovu 5, Praha 121 16, Czech Republic
[b] Research Centre, University of Žilina, Univerzitná 8215/1, Žilina 010 26, Slovakia
[c] Institute of Plasma Physics of the Czech Academy of Sciences, Za Slovankou 1782/3, 182 00 Praha 8, Czech Republic
[d] Institute of Machine and Industrial Design, Brno University of Technology, Technická 2896/2, Brno 616 69, Czech Republic

Received 29 January 2024; received in revised form 28 February 2024; accepted 7 April 2024
Available online 27 April 2024

Abstract

This work explored possibilities of biodegradable magnesium alloy Mg-3Y preparation by two modern powder metallurgy techniques – spark plasma sintering (SPS) and selective laser melting (SLM). The powder material was consolidated by both methods utilising optimised parameters, which led to very low porosity (∼0.3%) in the SLM material and unmeasurably low porosity in the SPS material. The main aim of the study was the thorough microstructure characterisation and interrelation between the microstructure and the functional properties, such as mechanical strength, deformability, and corrosion resistance. Both materials showed comparable strength of ∼110 MPa in tension and compression and relatively good deformability of ∼9% and ∼21% for the SLM and SPS materials, respectively. The corrosion resistance of the SPS material in 0.1 M NaCl solution was superior to the SLM one and comparable to the conventional extruded material. The digital image correlation during loading and the cross-section analysis of the corrosion layers revealed that the residual porosity and large strained grains have the dominant negative effect on the functional properties of the SLM material. On the other hand, one of the primary outcomes of this study is that the SPS consolidation method is very effective in the preparation of the W3 biodegradable alloy, resulting in material with convenient mechanical and degradation properties that might find practical applications.

Keywords: Magnesium; Yttrium; Powder metallurgy; Microstructure; Mechanical strength; Corrosion resistance.

1. Introduction

Magnesium (Mg) and its alloys have garnered considerable interest in recent years as promising materials for various engineering applications due to their exceptional combination of low density, high specific strength, and excellent machinability. Magnesium alloys also combine superior biocompatibility, mechanical properties close to human bones, and natural biodegradability. Biodegradable magnesium devices and implants are therefore believed to become a cost-effective option for medical implants in the future [1]. Among the myriad of magnesium alloys, those incorporating yttrium (Y) as an alloying element have been subject to extensive investigation, as Y is biocompatible [2,3] and can significantly enhance the mechanical and corrosion properties of Mg-based materials [4,5]. Yttrium was found to be an excellent element for improving mechanical properties both at ambient and elevated temperatures due to the solid solution strengthening [6]. Moreover, yttrium was reported to play a crucial role in

* Corresponding author at: Faculty of Mathematics and Physics, Charles University, Ke Karlovu 5, Praha 121 16, Czech Republic.
E-mail addresses: peter.minarik@mff.cuni.cz, peter.minarik@uniza.sk (P. Minárik).

https://doi.org/10.1016/j.jma.2024.04.018

moderating corrosion resistance [7]. There are two significant effects on corrosion resistance resulting from yttrium incorporation: firstly, yttrium shows a high solubility in the Mg matrix, preventing undesirable galvanic corrosion between the Mg matrix and intermetallic phases [8]. Secondly, during corrosion, a dense protective film of Y_2O_3 is formed, effectively slowing down or suspending the corrosion attack [5].

The Mg-3Y alloy was investigated in our previous study and it was shown that it is a good candidate for the medical applications. The alloy exhibited a very good combination of strength, ductility, and *in vitro* degradation properties, especially in the ultrafine-grain state prepared by equal channel angular pressing [9]. In this study, we turn our focus on two innovative powder metallurgical techniques – spark plasma sintering (SPS) and selective laser melting (SLM). Both of these techniques provide a relatively easy and time-effective method for preparing near-net-shape implants; therefore, they are of high interest to modern medicine [10,11].

The SPS process involves the application of high temperature and pressure in a fast and energy-efficient manner, resulting in rapid powder consolidation and excellent material properties [12]. The electrical current passes through the conductive die and the powder, generating localised heating at the powder particle contacts. Before the actual sintering begins, pressure is applied to the powder inside the die, which helps to eliminate any voids or porosities within the powder bed and ensures uniform densification during the sintering process. Unlike traditional sintering methods, SPS heats the material internally, which enables quicker heating rates and reduces the overall processing time [13].

The SLM process belongs to the family of additive manufacturing techniques, which are commonly addressed as 3D printing [10]. This process involves joining metal powder to build a 3D object layer by layer, based on a digital 3D model. SLM utilises a high-powered laser beam to melt and fuse the metal powder. After completing each layer, the printer adds a new layer (powder bed), continuously building the 3D object. The advantages of SLM are design flexibility, material efficiency, and the ability to create complex geometries suitable for medical applications [14].

During the last decade, several magnesium alloys have been prepared by SPS and/or SLM techniques with different results, commonly depending on the alloy composition [10,12,15–18]. The key factor, which generally has a strong impact on the physical properties of the compacts, is the residual porosity. For both manufacturing methods, there is some general knowledge regarding the effects of the individual processing parameters on the resulting microstructure, but they need to be tailored for each alloy separately to prepare the compacts with favourable properties.

This paper presents a systematic comparative investigation of the microstructure, mechanical properties, and corrosion resistance of the binary Mg-3Y magnesium alloy processed using three different techniques: Selective Laser Melting, Spark Plasma Sintering, and Extrusion. Extrusion is a common manufacturing process used to create objects with a fixed cross-sectional profile by forcing a material through a specially designed die or a set of dies. This technique is well-known and presents a benchmark for the two powder metallurgy techniques. It is important to note that each of these processes has a distinct effect on the microstructure, which subsequently affects the mechanical and corrosion properties of the alloy [9]. A comprehensive comparison of these three processing techniques concerning their influence on the mechanical and corrosion properties of the biodegradable Mg-3Y alloy provides important insights on its utilisation, especially in medical applications.

2. Materials and methods

2.1. Initial material

In this work, Mg-3Y alloy (wt.%, W3) was cast from pure elements and subsequently gas-atomised at Nanoval GmbH & Co. KG, Berlin. The obtained powder was sifted and the resulting D50 value was 41 μm. The powder was prepared under an inert atmosphere and all powder handling was carried out in a low-oxygen environment to prevent oxidation.

The SEM micrographs showing the microstructure of the powder particles are presented in Fig. 1. The powder particles exhibit a round shape with occasional deformations (Fig. 1a). An inner structure of the powder particles exhibited a typical dendritic structure (Fig. 1b) resulting from the rapid cooling [19]. The brighter areas correspond to a higher concentration of heavier yttrium atoms due to the compositional contrast, as shown in Fig. 1c (top) and confirmed using energy-dispersive X-ray spectroscopy (EDS) (bottom). An electron back-scatter diffraction (EBSD) analysis of the powder microstructure (Fig. 1d) revealed that the grain distribution strongly depends on the size of the individual particles. Smaller particles contained only one or a few grains, while larger particles consisted of many grains.

2.2. Processing

The specimens from gas-atomised W3 powder were fabricated by the Laser Powder Bed Fusion process. A 3D printer SLM 280HL (SLM-Solutions AG, Germany) was used for this purpose. The machine featured a 400 W YLR-Laser (IPG Photonic) with a Gaussian profile and a spot size diameter of approx. 82 μm. To prevent oxidation or burning of the powder during the application of the laser beam, the building chamber was filled with an inert argon atmosphere with an oxygen level below 0.2%.

The optimal processing parameters were established by a series of experiments, starting from the fabrication and evaluation of single weld tracks, followed by a series of volumetric specimens in the form of 10 × 10 × 10 mm^3 cuboids. For all experiments, 50 μm layer thickness was used. Using single weld tracks, 90 combinations of processing parameters with variations of Laser Power (LP) and Scanning Speed (SS) were evaluated. The parameters were set within the range of LP = 60–240 W and SS = 200–1500 mm/s. Single weld tracks were evaluated with regard to weld track continuity

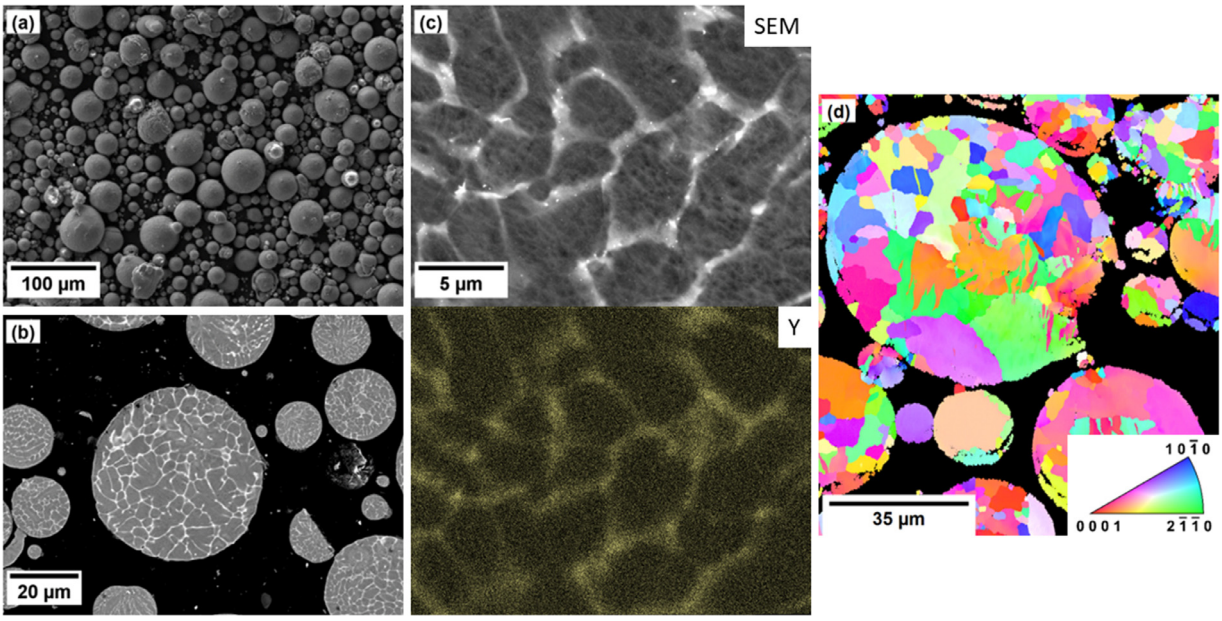

Fig. 1. Gas-atomised powder: (a) SEM micrograph, (b) SEM cross-section, (c) detail of dendritic microstructure with Y elemental map of the same area, and (d) EBSD orientation map.

using a light microscope Keyence VHX 6000, followed by a more detailed evaluation of weld track cross-section by metallography, considering only continual tracks of good quality. Based on the weld track width, depth, and the presence of defects, 10 of the best combinations of processing parameters were chosen for volumetric testing with cuboid specimens. The cuboid experiments consisted of several iterations evaluated by metallography in the XY cross-section (parallel to the baseplate, Fig. 2), while the variation in hatching distance (HD) with a resulting overlap of 30–50% between individual weld tracks was used. The best combination was found as LP = 180 W, SS= 600 mm/s, HD = 0.09 mm. Cuboids fabricated with such parameter combinations showed a relative density of 99.8% in XY and XZ sections. Based on small cuboid samples, rectangular specimens with dimensions of $20 \times 10 \times 6$ mm^3 were produced (schematically drawn in Fig. 2).

Spark Plasma Sintering (SPS) was selected as a second way of consolidating the W3 powder. The consolidation was performed in a Thermal Technology LLC device type 10–4. 10 g of the powder was used for one sample. Sintering was conducted in the cylindrical graphite tool at 550 °C for 10 min under a pressure of 100 MPa. These processing parameters for SPS were selected based on our previous results, for details see Refs. [12,20]. Utilisation of these parameters resulted in unmeasurably low residual porosity. The temperature was controlled by a thermocouple placed inside the graphite tool. A protective argon atmosphere was used to prevent oxidation. The resulting sample had a diameter of 30 mm and a height of 8 mm (schematically drawn in Fig. 2).

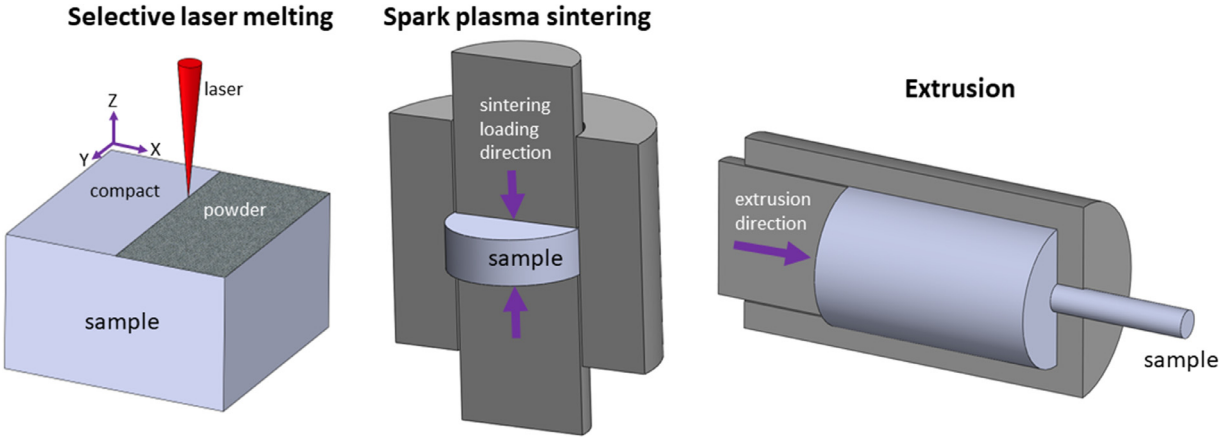

Fig. 2. Schematic illustration of selective laser melting (SLM), spark plasma sintering (SPS) and extrusion process (EX), together with major sample directions. SLM orientation is denoted through the text according to the coordinate system, SPS according to the sintering loading direction (SLD), and EX according to the extrusion direction (ED).

Finally, the third W3 material was prepared by means of extrusion. Before extrusion (EX), the cast billet was homogenised at 400 °C for 16 h. Subsequently, the billet was extruded at 350 °C with an extrusion ratio (ER) of 30 and an extrusion rate (ram speed) of 3 mm/s, as schematically drawn in Fig. 2. The diameter of the extruded rod was 17 mm.

2.3. Microstructure

The microstructure of the gas-atomised powder and the prepared materials were analysed using the scanning electron microscope (SEM) ZEISS Auriga Compact equipped with the EDAX EDS and the EDAX EBSD camera. The relative porosity of the samples prepared via powder metallurgy was also determined from high-resolution SEM images as the surface fraction of the polished specimens. At least 10 images with suitable magnification were analysed for this purpose. The samples for SEM investigation were mechanically polished with the decreasing abrasive grain size down to 50 nm. Samples for EBSD were subsequently ion-polished using a Leica RES102 device. The EBSD analysis was performed on the area of 2 × 2 mm^2 with a step size of 2 μm to acquire sufficient datasets for all statistical calculations in the TSL OIM 8 software. The measured data were partially cleaned by one step of confidence index (CI) standardisation and one step of grain dilatation. Only points with CI > 0.1 were used for the analysis.

A transmission electron microscope (TEM) JEOL F2000FS equipped with Bruker EDS was used for precise identification of the secondary phase particles. As samples for TEM, discs of 3 mm in diameter were cut from the investigated materials, mechanically thinned down to 150 μm, and finally ion-polished to electron-transparent thickness.

2.4. Mechanical properties

The mechanical properties of the manufactured materials were studied through Vickers microhardness tests (HV), compressive, and tensile deformation tests. The QNESS Q50 device was used for Vickers microhardness tests, calculating the average microhardness from at least 150 indents. The deformation tests were performed using the Instron 5882 universal testing machine at room temperature with a constant crosshead speed, providing an initial strain rate of 10^{-3} s^{-1}. The tensile samples had a flat dog-bone shape with gauge dimensions of 8 × 4 × 1.5 mm^3, while the dimensions of the compression samples were 5 × 3 × 3 mm^3. At least three tests were performed for each condition.

For the digital image correlation (DIC) measurements, the tensile samples were ground using #1200 SiC emery paper followed by the application of fine speckle pattern by means of the airbrush technique utilising water-based paints. The sample images were captured during loading at a rate of 1 fps using the Nikon D3100 camera. The DIC data were evaluated using the Ncorr package implemented in Matlab [21]. The same DIC parameters were used for all samples: subset radius of 40 px, subset spacing of 5 px and strain radius of 4 points.

2.5. Corrosion resistance

A linear polarisation method was used to study the initial corrosion resistance of the studied materials. The tests were conducted with the potentiostat Metrohm AUTOLAB128N using the three-electrode setup. The polarisation curves were measured after 10 min of stabilisation in 0.1 M NaCl aqueous solution at room temperature. The measurement was performed from −150 mV to 200 mV vs. the open circuit potential (OCP) with the scan rate of 1 mV/s. A rotating disc electrode (sample) was used for better homogeneity of the measurement, using 300 rpm. The samples were cut in the YZ plane (X-direction) and, prior to each measurement, the exposed surface was ground with #1200 SiC emery paper and rinsed with ethanol. The values of corrosion potential (E_{corr}), corrosion current density (i_{corr}) and polarisation resistance (R_p) were determined from the measured data by the Tafel analysis.

The long-term corrosion performance of the studied materials was evaluated through weight loss measurements. Specimens with dimensions of 1 × 6 × 6 mm^3 (XYZ) were cut from each material, and their initial weight m_0 was recorded. Subsequently, these samples were submerged in a 0.1 M NaCl aqueous solution for a duration of 7 days. Following this immersion period, the specimens were carefully removed from the solution, and the corrosion products were removed according to the ISO 8407:2009 standard. Upon cleaning, the weight of each sample m was remeasured, and the corrosion rate CR was calculated using the formula: $CR = (m_0 - m) / (t \cdot S)$, where t represents the immersion time and S denotes the total surface area of the sample. At least three samples were examined for each type of material.

3. Results

3.1. Microstructure

Fig. 3 shows an overview of the microstructure of the investigated materials in terms of SEM micrographs. Both materials prepared via powder metallurgy exhibited compact structure, however, the inner structure, especially with an emphasis on the distribution of the secondary phases, was significantly different. The bright secondary phase particles are distributed relatively uniformly in the magnesium matrix of the SLM sample (Fig. 3a). On the other hand, the SPS sample clearly exhibits distinguishable former powder particles surrounded by a continuous bright layer, as documented in Fig. 3b. In addition, small discontinuous precipitates inside the former powder particles and clearly depleted zones along the earlier powder particle boundaries were formed, marked by red lines (detail in Fig. 3b). As mentioned above, the processing method also had a strong impact on the residual porosity. A low residual porosity of ~0.3% was measured in the SLM sample by SEM image analysis of both investigated planes. On the other hand, no residual porosity was observed in the material prepared by SPS. These results correspond well with the aforementioned investigation performed

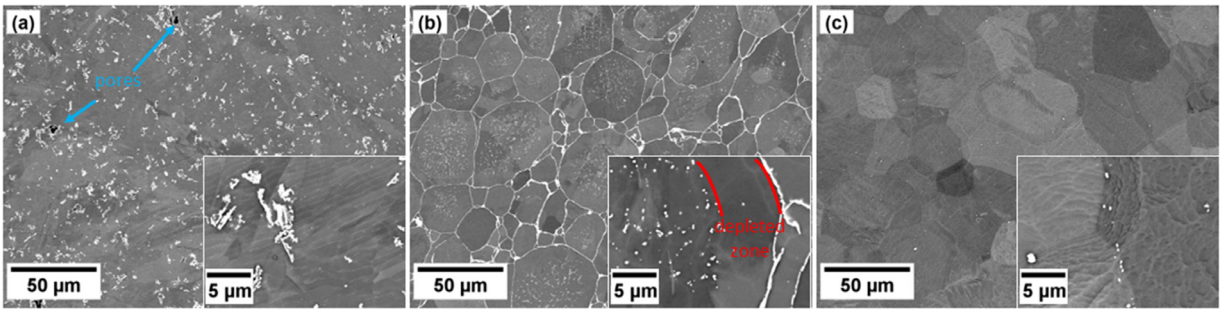

Fig. 3. SEM micrographs of the microstructure of (a) SLM sample, (b) SPS sample, and (c) EX sample.

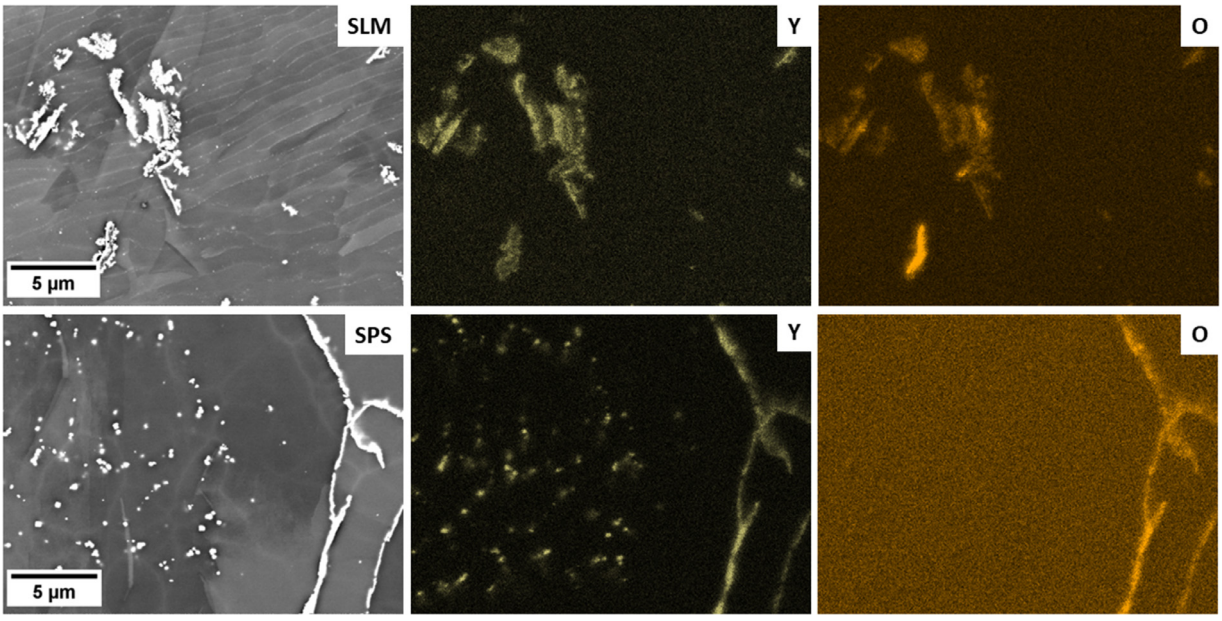

Fig. 4. SEM micrographs and corresponding elemental distribution maps for Y and O measured in SLM and SPS samples.

by light microscopy during the optimisation of SLM parameters. Fig. 3c presents the microstructure of the EX condition. Because of the highly limited presence of any secondary phase particles, it is clear that almost all yttrium is dissolved in the magnesium matrix. The occasional small bright particles were identified in our previous investigations as the stable $Mg_{24}Y_5$ phase [22].

The secondary phase characterisation in SLM and SPS samples was performed via a combination of EDS chemical mapping (Fig. 4) and selected area diffraction (SAED) pattern analysis in TEM (Fig. 5). The EDS maps showed that the secondary phase particles in both materials contain yttrium, and some of them also oxygen. The dominant secondary phase particles in the SLM sample have a fine "curtain-like" character and contain both yttrium and oxygen (Fig. 4). According to the subsequent TEM analysis, these particles are the nanocrystalline Y_2O_3 phase (Fig. 5a). Their shape and distribution strongly suggest that these oxides formed on the outer shell of the former powder particles during gas-atomisation, which were abruptly disrupted during the SLM process. TEM investigation also revealed the presence of the $Mg_{24}Y_5$ phase, however, the number of these particles was very low (Fig. 5a). The Y_2O_3 phase in the SPS sample forms a continuous 3D net along the former powder particle boundaries, as disclosed in Figs. 4 and 5b. Its form is nanocrystalline, similar to the SLM sample, proving that this oxide was formed already on the initial powder particles during gas-atomisation. Nevertheless, the concentration of yttrium along these former powder particle boundaries was much higher than the Y/O ratio corresponding to the Y_2O_3 phase. Therefore, the depletion of yttrium from the magnesium matrix along these boundaries (Fig. 3b) is caused by its segregation into these boundaries. The fine precipitates inside the former powder particles do not contain oxygen (Fig. 4) and were identified as the YH_2 phase (Fig. 5c). Occasional presence of larger clusters of crystalline (200 nm) Y_2O_3 phase particles was found in TEM samples of both materials (Fig. 5c). Based on their type and shape, they are considered to be residuals from the casting process prior to atomisation.

The grain structure of all investigated materials was thoroughly examined using EBSD. The orientation maps of the SLM and SPS samples were measured in two different planes, the top plane and the side plane, to investigate a possible anisotropy of the grain structure. All orientation maps are

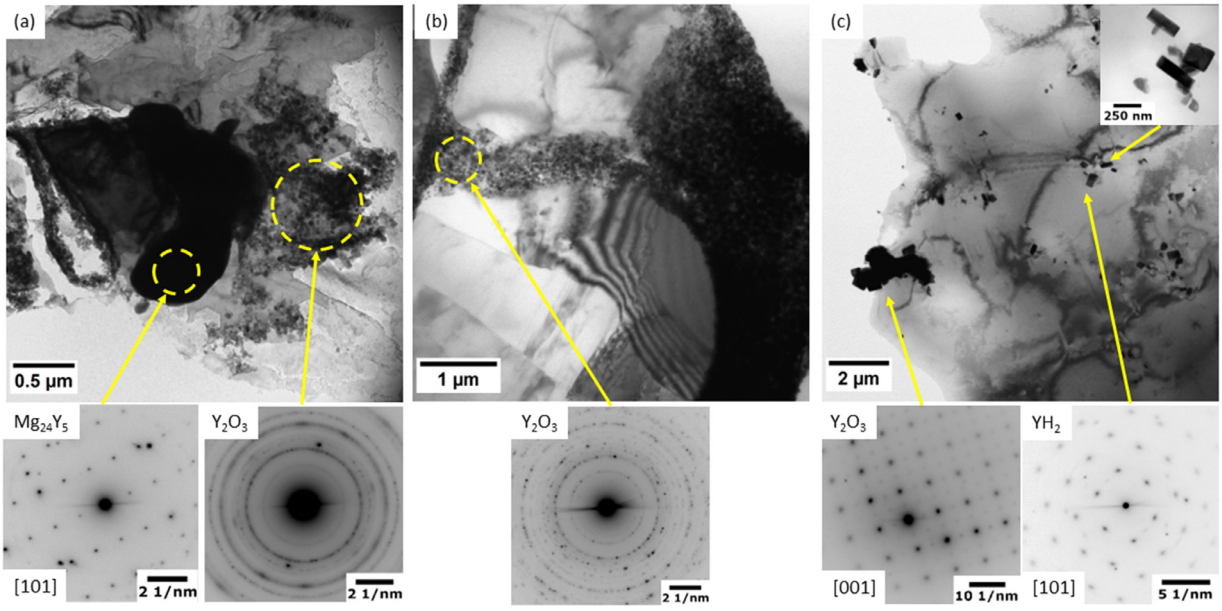

Fig. 5. TEM micrographs of (a) SLM sample and (b, c) SPS sample with corresponding SAED patterns.

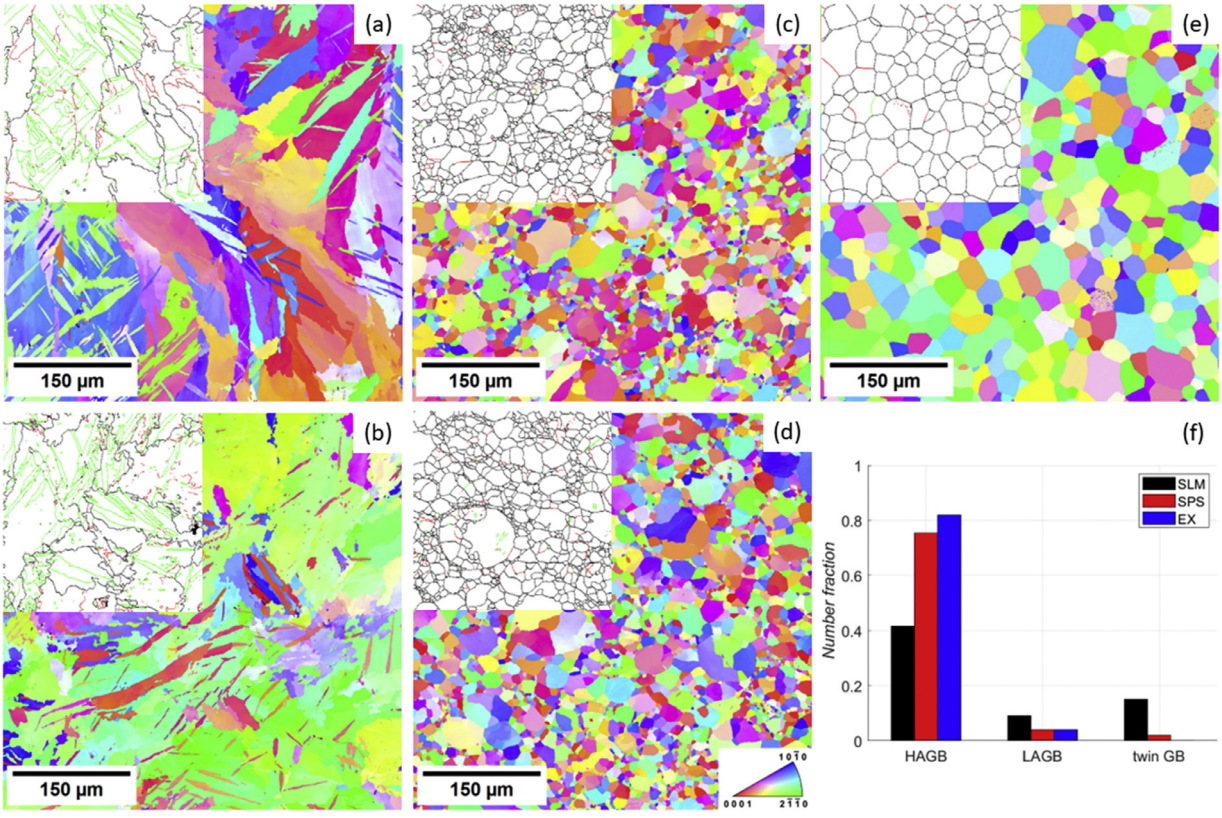

Fig. 6. EBSD orientation maps of the microstructure of (a) SLM top section (Z-direction), (b) SLM side section (X-direction), (c) SPS top section (SLD), (d) SPS side section, (e) EX samples (ED) and (f) distribution of grain boundaries type. (a-e) overlays: black – HAGBs, red – LAGBs, green – twin GBs.

shown, together with the EX sample (only perpendicular to ED), in Fig. 6. According to the micrographs, there is little difference between the two sections of the individual samples. Nevertheless, there is a significant difference in the grain structure resulting from the different processing methods. The SLM sample is formed by relatively large grains containing a high number of twins (Fig. 6a and 6b). The grains are prolonged to several hundreds of microns, have curly grain boundaries, and the colour variation within the grains indicates a relatively high residual strain. The character and

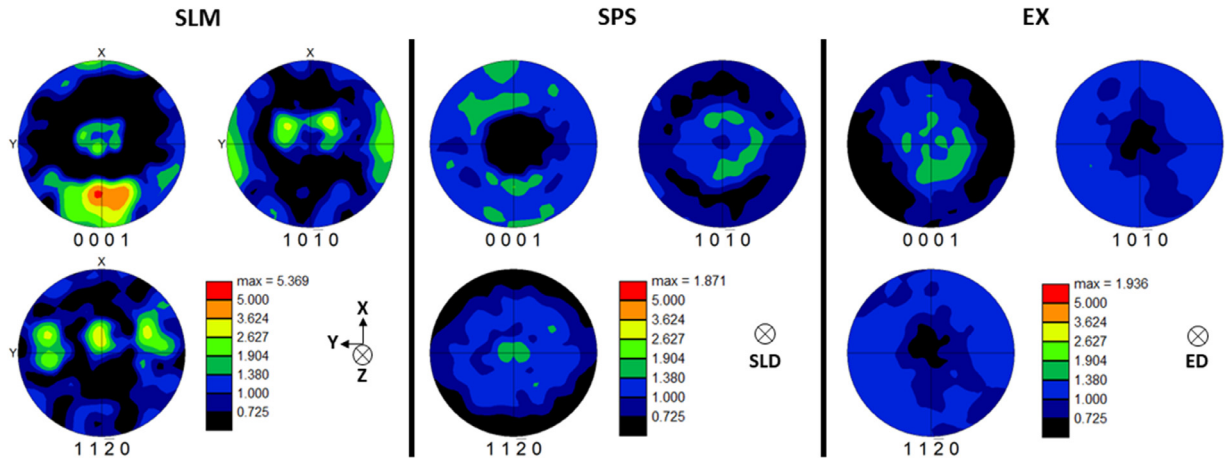

Fig. 7. EBSD pole figures calculated for the investigated samples.

distribution of the twin boundaries and low/high angle grain boundaries (LAGB/HAGB) are depicted in overlays. Note that the low- and high-angle grain boundaries had misorientation limitations set to be 2°−15° (LAGB) and >15°. The overall number fraction of each grain boundary type is shown for all samples in Fig. 6f.

The SPS resulted in a significantly different grain structure. Fully recrystallised equiaxed grains with insignificant residual strain, a low fraction of LAGBs and only a negligible fraction of twin boundaries were observed in this material (Fig. 6c and 6d). The average grain size was calculated to be ∼20 μm. The grain boundary maps reveal that the final grain structure after SPS is partially related to the initial powder particle shape. Locally, the grain growth through the former powder particle boundaries was hindered due to the presence of an oxide layer.

The EX material exhibited a fully recrystallised grain structure with equiaxed grains of ∼32 μm in diameter. No twin boundaries and only a low number fraction of LAGB were observed.

The texture analysis results, in the form of EBSD pole figures, are shown in Fig. 7. Interestingly, the EX and SPS samples showed only a very weak texture (Fig. 7). In the SPS sample, the texture is {0001} basal texture parallel to the sintering loading direction, and in the EX sample, it is {11–20} fibre texture parallel to the ED. The texture strength in these two samples was below 2 times random. A significantly stronger texture was measured in the SLM sample. The orientation of the dominant component is close to {11–20}<10–10> parallel to the Z direction, and its strength is ∼5 times random.

3.2. Mechanical properties

The impact of microstructural differences resulting from different processing techniques on the mechanical strength was at first investigated using Vickers microhardness testing. In the case of the SLM sample, the microhardness was measured in two planes (XY, YZ) in order to reveal potential anisotropy with respect to the building direction. The tests revealed that all samples, including the two planes in the SLM sample, exhibited uniform microhardness distribution over the measured areas; the resulting average values are summarised in Table 1. All three microstructural conditions prepared by different methods resulted in very similar microhardness (∼50 HV). Furthermore, no anisotropy was observed in the SLM sample as microhardness values measured in XY and YZ planes of the SLM sample agree within the statistical error.

Table 1
Vickers microhardness of all the investigated samples.

Material	microhardness [HV]
SLM (XY plane)	50.0 ± 4.7
SLM (YZ plane)	52.0 ± 3.5
SPS	49.9 ± 1.7
EX	57.0 ± 3.0

The compressive and tensile deformation tests were performed to reveal the mechanical response of the investigated samples under uniaxial load. The sample orientation was the same for tensile/compressive tests: parallel to X direction for the SLM sample, perpendicular to SLD for the SPS sample and parallel to ED for the EX sample. DIC was also performed to observe strain distribution during tensile tests. The true plastic stress-strain curves for compressive and tensile tests are presented in Fig. 8.

The compressive deformation curves displayed a sigmoidal shape (Fig. 8a) for all samples, indicating activity of the {10–12} mechanical twinning during compression [23,24]. In contrast, the tensile tests exhibited a power-law curve typical of deformation mediated solely by dislocation slip (Fig. 8b) [25]. Mechanical parameters evaluated from the deformation curves, namely the compressive and tensile yield strength, ultimate tensile strength, and elongation to fracture, are presented in Table 2. Note that the elongation to fracture was evaluated from the DIC data and represents the maximal elongation in tension before specimen fracture.

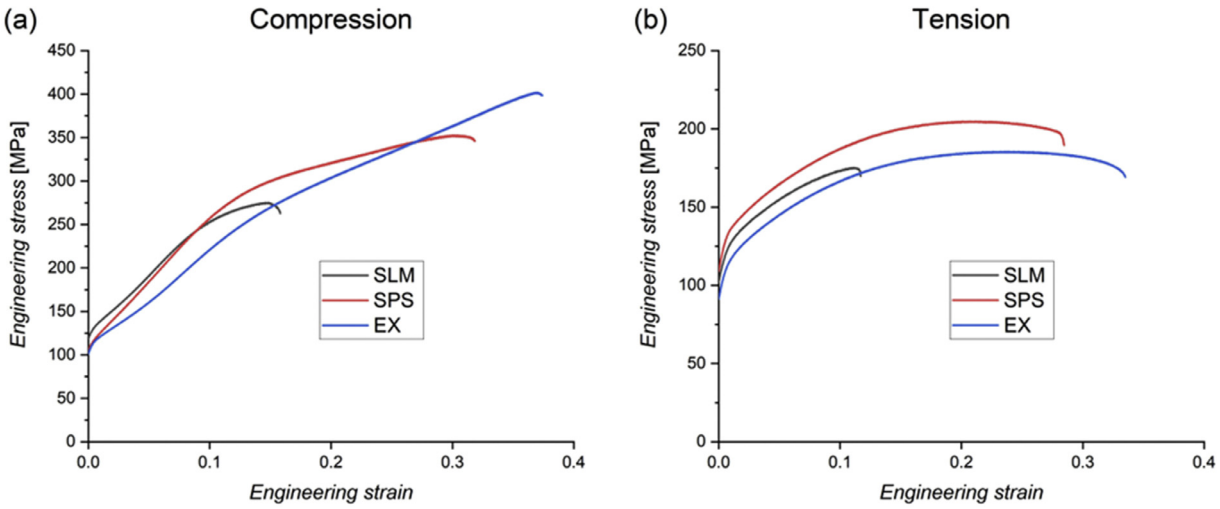

Fig. 8. The representative true stress-strain (a) compressive and (b) tensile curves of the SLM, SPS and extruded samples. Note different y-axis.

Table 2
The mechanical parameters (compressive/tensile yield strength - CYS/TYS, ultimate tensile strength – UTS, and fracture elongation in tension - ε_{max}).

Material	SLM	SPS	EX
CYS [MPa]	117 ± 7	108 ± 3	107 ± 3
TYS [MPa]	113 ± 3	115 ± 2	99 ± 1
UTS [MPa]	180 ± 4	200 ± 3	186 ± 1
ε_{max} [%]	9 ± 1	21 ± 3	30 ± 3

Despite the different microstructures, the resulting yield stress values are very similar for all studied conditions and both deformation directions. In compression tests, the major difference in the samples lies in the magnitude of twinning (more pronounced sigmoidal curve in the case of the EX material) and in the deformation to fracture. In the tensile tests, the strengthening rate is similar for all three materials, but the fracture elongation differs significantly. The SLM sample exhibited lower UTS and ε_{max} (180 MPa, 9%) compared to both SPS (200 MPa, 21%) and EX (186 MPa, 30%) materials.

Fig. 9 shows the evolution of strain distribution of all the sample types during tension up to 1% before fracture calculated using the DIC technique. The least ductile SLM sample developed considerable strain localisation as early as at 1% global plastic strain in terms of several highly strained deformation bands and spots. Subsequently, some of these sites evolved into the critical crack, leading to failure, as marked with two white ellipses in Fig. 9. On the other hand, the SPS and EX samples exhibited much more homogeneous local strain evolution up to higher global strains, although they differed in the critical crack initiation. Specifically, in the case of the SPS sample, the strain distribution was homogeneous up to at least 15% of global strain, and a distinct critical crack formed at the edge of the sample only shortly before failure. The most ductile EX sample exhibited homogeneous local strain up to 15%, too, however, the crack formation was preceded by the characteristic necking: some strain localisation in the central part of the sample occurred already at 22% of global strain and was followed by a development of distinctive neck identified before failure. Both the nature of the fracture and the strain localisation were consistent for all measured samples of the given material set.

The origin of the strain localisation in the SLM sample and, particularly, in the weak spots 1 and 2 (cf. Fig. 9) was revealed by the observation of fracture surfaces by SEM, see Fig. 10a and b. The fracture morphology and only limited signatures of plasticity (plastic dimples) confirm that the fracture took place in a brittle manner. The fracture surfaces of SPS and EX samples are shown in Fig. 10c and d, respectively. The fracture surface of the SPS sample contains signatures of intensive plastic deformation and almost no silhouettes of the original powder particles. In the case of the EX sample, the analysis of the fracture surface revealed both the presence of intergranular fracture without visible plastic dimples, as well as severely plastically deformed areas.

3.3. Corrosion resistance

The linear polarisation tests were conducted on all studied materials to investigate the initial susceptibility (10 min of stabilisation) of the samples to the corrosion attack in 0.1 M NaCl aqueous solution. The corresponding curves are presented in Fig. 11. Notably, all polarisation curves showed a similar shape, and the most pronounced difference is the shift of the corrosion potential (E_{corr}) of both powder metallurgy samples towards less noble values compared to the extruded sample. The corrosion current density (i_{corr}) evaluated according to the Stern analysis was the same for the SPS and extruded samples, while the SLM sample showed a little lower corrosion current density, see Table 3.

To further examine the corrosion behaviour of the investigated samples, 7-day immersion tests were conducted, and the corresponding corrosion rates were calculated. The corrosion rates of the studied materials are presented in Table 3. From the results, it is evident that the extruded and SPS materials exhibited similar corrosion rates within the error. On the

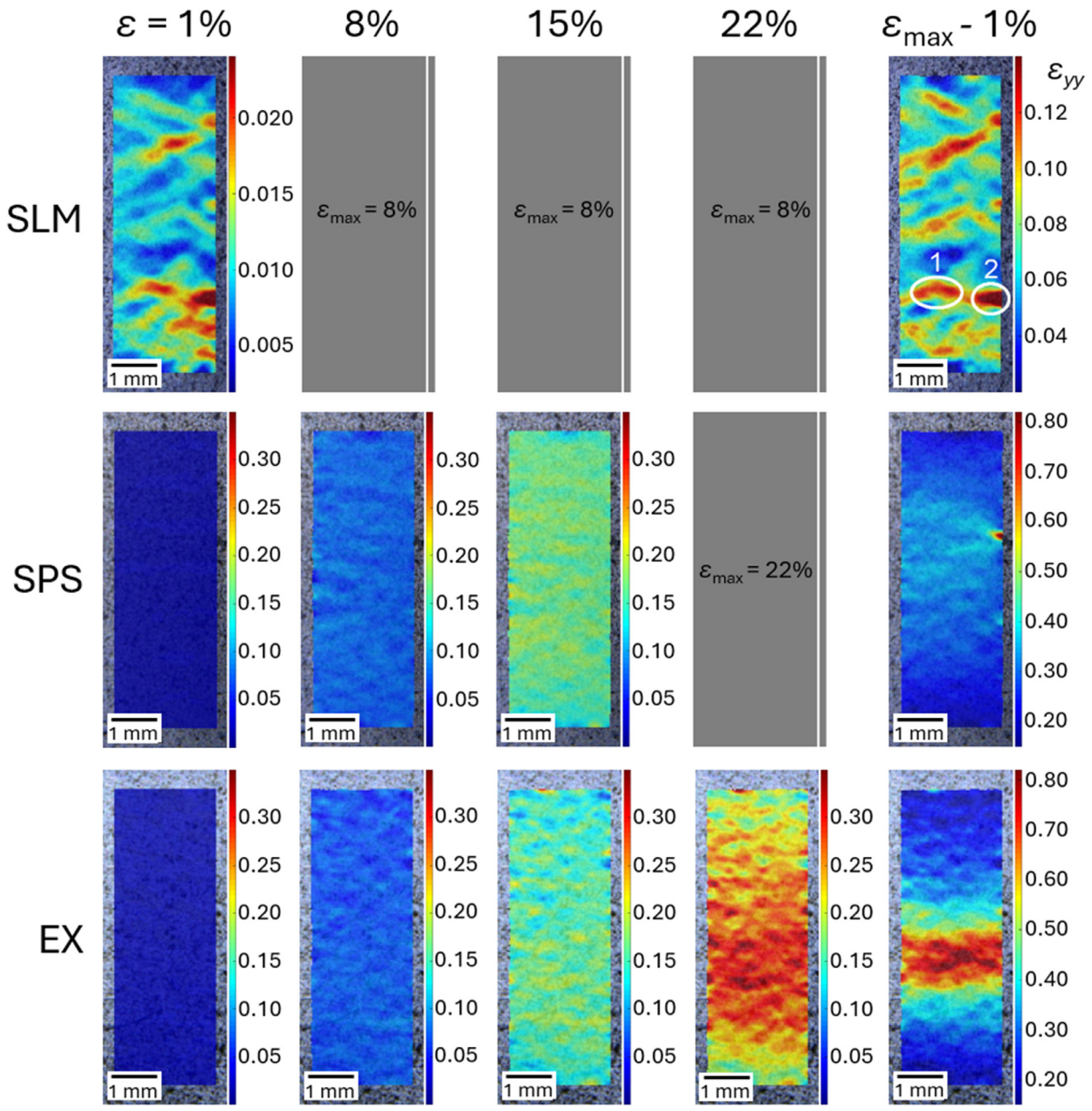

Fig. 9. The DIC results show the evolution of strain distribution during tensile tests in terms of Lagrangian strains (ε_{yy}) in the loading, i.e. vertical, direction for all three types of materials. ε_{yy} was evaluated at several points of global strain (ε) depending on the fracture strain ε_{max} of particular material: SLM – 1% and 1% before fracture (∼7%), SPS – 1%, 8%, 15%, and 1% before fracture (∼21%), EX – 1%, 8%, 15%, 22%, and 1% before fracture (∼29%). Note different colorbar scales throughout the figure.

Table 3
The corrosion characteristics determined from Fig. 11 and corrosion rate (CR) evaluated from the immersion test for all investigated samples.

Material	SLM	SPS	EX
E_{corr} [V vs. SCE]	−1.620 ± 0.004	−1.620 ± 0.003	−1.604 ± 0.003
i_{corr} [mA·cm^2]	0.34 ± 0.03	0.45 ± 0.03	0.46 ± 0.02
CR_{icorr} [mg·cm^2·h^{-1}]	0.15 ± 0.01	0.20 ± 0.01	0.21 ± 0.01
CR [mg·cm^2·h^{-1}]	> 0.603*	0.19 ± 0.02	0.17 ± 0.01

* estimated degradation within 5 days of immersion.

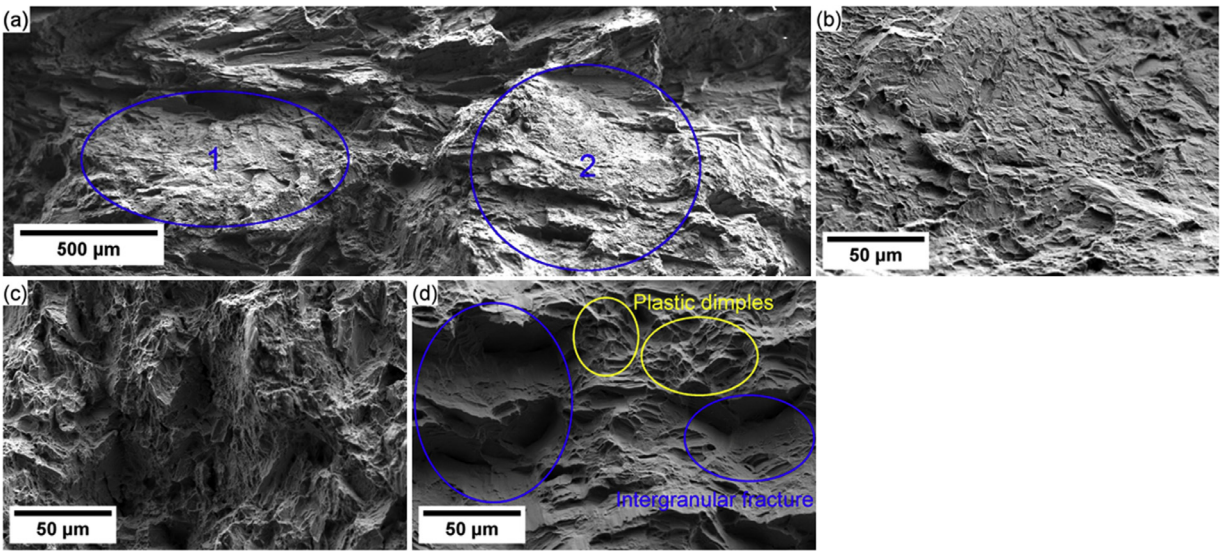

Fig. 10. Fracture surfaces of tensile specimens (a) SLM sample – low magnification, (b) SLM sample – detail (area 2), (c) SPS sample and (d) EX sample.

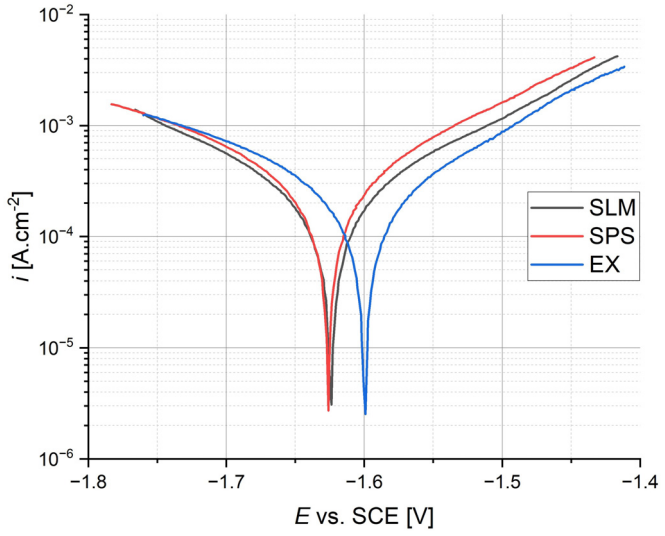

Fig. 11. Tafel polarisation curves of the investigated samples.

other hand, the SLM material displayed severe degradation and, therefore, a high corrosion rate. Note that the calculated value is based only on the 5-day experiment because, after 7 days, the sample lost its structural integrity.

Fig. 12 presents the SEM cross-sections of the corrosion surface layer developed on the investigated materials after 4 days of immersion in 0.1 M NaCl solution. It is evident that the severity of the corrosion attack was significantly dependent on the preparation method. Both SPS and EX samples exhibited relatively uniform propagation of corrosion into the material and a relatively compact surface film of the corrosion products. While in the EX sample, no microstructural features clearly interacted with the propagation of the corrosion front, a significant effect of the former powder boundaries enriched by Y is visible in the SPS sample. The boundaries substantially hinder the corrosion attack when they are oriented relatively parallel with the corrosion front (indicated by red arrows in Fig. 12b). The most severe attack was observed in the SLM sample. The corrosion front was highly uneven, the surface film was full of cracks, and large pieces of the corrosion products had detached.

4. Discussion

4.1. Microstructure

The final microstructure of materials prepared by both SLM and SPS is always strongly related to the alloy composition and used processing parameters [10,12,15–18]. It needs to be noted that the processing parameters employed in this study were selected based on intensive previous research and resulted in excellent consolidation in the case of both powder metallurgy techniques. The fine-tuning of both SLM and SPS processing parameters resulted in a very low residual porosity, which was only ~0.3% in the case of SLM and below the resolution of SEM in the case of SPS. This result is superior in comparison to the literature, where the residual porosity of magnesium materials is often reported to be significantly higher for both processing techniques [15,16,18,26,27].

The initial microstructure characterisation by SEM revealed that the utilisation of both powder metallurgy techniques led to the presence of a relatively high volume fraction of oxides in the consolidated samples. The dominant phase was nanocrystalline Y_2O_3, which forms on the powder particles already during atomisation as a stabilising oxide. Note that the formation of Y_2O_3 is preferred compared to the MgO in this alloy because Y_2O_3 has a lower Gibbs energy than MgO, for details see e.g. [28]. The major difference between the two consolidation techniques was the final spatial distribution of the oxide particles. The positive impact of the SLM over the SPS processing is the disruption of this oxide film and the formation of very fine “curtain-like” particles present

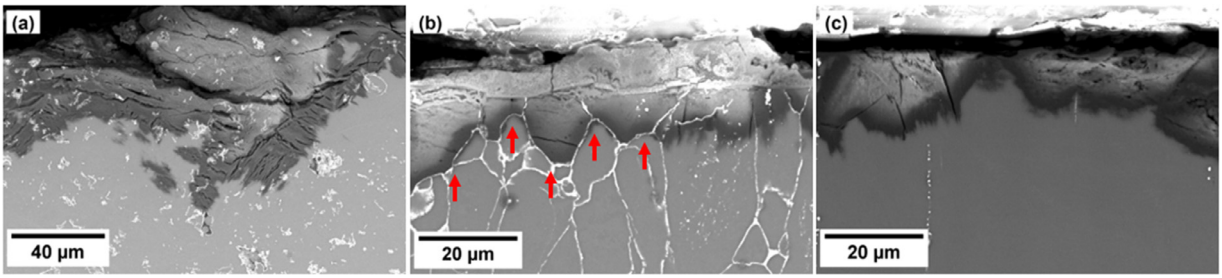

Fig. 12. SEM micrographs of cross-sections of the corrosion surface layer developed on the investigated materials after 4 days of immersion in 0.1 M NaCl solution. (a) SLM, (b) SPS, and (c) EX sample. Note different magnification.

in the magnesium matrix, see Fig. 3. The local melting of the powder particles and the formation of a travelling melt pool causes convection, which disrupts thin oxide shells [29,30]. Therefore, the spatial distribution of the oxides is random in the SLM sample, while in the SPS sample, the oxides formed a 3D net-like structure along the former powder particles. Its origin lies in the fact that consolidation of the powder during SPS does not include complete melting of the powder particles; moreover, there is no liquid flow of the material. This oxide superstructure is a typical feature observed in a variety of Mg alloys prepared by SPS, repeatedly reported in different studies [18,31].

Nevertheless, the compactness of the oxide superstructure observed in SPS sample was significantly different to the majority of other similarly processed Mg alloys. Commonly, a relatively thick MgO shell forms on the powder particles during atomisation, which limits diffusion during sintering. As a result, the interconnection of the individual powder particles in the sintered samples is poor. In our recent studies, we have shown that the presence of dissolved rare earth elements in the magnesium matrix, in particular yttrium and neodymium, together with high applied force during SPS, may cause enhanced segregation of these elements into the former powder boundaries. Consequently, partial melting along the former powder boundaries occurs because of locally shifted composition towards the eutectic point. Finally, the partial melting causes disruption of the oxide shell and better interconnection between the powder particles after sintering, for details see [19,20]. This effect may be directly observed in Figs. 3b and 4, in which clear depletion of yttrium along the former powder boundaries is associated with its increased content in these boundaries. Consequently, the negative effect of the 3D net-like nanocrystalline oxide on mechanical properties is significantly suppressed by its disruption, as discussed later.

The other very important difference between the SLM and SPS samples lies in the formation of the $Mg_{24}Y_5$ and YH_2 phases (Fig. 5). The $Mg_{24}Y_5$ phase was formed in the SLM sample in locations unrelated to the other microstructural features, and it is therefore considered that local fluctuations of Y during cooling were responsible for the occurrence of this phase [32]. On the other hand, in the SPS sample, this phase was not observed even in the former powder boundaries, in which an increased amount of Y was measured. Note that the cooling rate during the SLM process is much slower than during the SPS and, in addition, the same volume is repeatedly thermally affected by the successive laser passes during the sintering of the following layers of the material. Instead, the YH_2 phase precipitated inside the former powder particles, as shown in Figs. 3 and 4. Rare earth elements, including yttrium, have a very high affinity to hydrogen, and this phase commonly forms when these alloys are exposed to hydrogen [33,34]. However, the reason why this phase precipitated only in the SPS sample is unknown, as the atmosphere during processing and powder handling before the consolidation were the same for both powder metallurgy techniques. In the case of the EX material, almost all yttrium was dissolved in the magnesium matrix because the processing temperature was above the $Mg_{24}Y_5$ phase solvus at this composition (~220 °C) and the material was rapidly cooled after the extrusion [22,32].

The EBSD analysis (Fig. 6) revealed the inner grain structure of the investigated samples and showed that powder melting and solidification during the SLM caused the formation of relatively large grains with high residual strain and twins. According to the literature, the processing parameters have a crucial effect on the final grain structure through the magnitude of the laser energy density and related cooling rate – the higher the laser energy density (lower cooling rate), the larger the grains [29,35–37]. There are reports showing very fine grain structures with an average grain size of less than 10 μm [29,35,37–44]. Nonetheless, in many papers, the grain size is usually considered only within the interdendritic region in a multiphase system, which is often misleading and yields significantly smaller value than the real grain size calculated by, e.g. EBSD analysis [45]. The only exceptions are highly alloyed AZ91D, WE43, Mg-10Gd-0.2Zr and Mg-15Gd-1Zn-0.4Zr, in which fine-grained microstructure (1–3 μm) was proved by the EBSD analysis [42,46–48]. It needs to be noted that our alloy contains a significantly lower amount of alloying elements, which would refine grain structure upon cooling, as this research was primarily focused on minimising the relative porosity with respect to the functional properties of the material. As mentioned above, the negligible porosity of the materials presented in this study surpasses the majority of the reported results [10,16]. The relatively high residual stress observed in Fig. 6 is a common problem associated with SLM-prepared materials because of the rapid melting and solidification cycles during the formation of each layer [49].

The mechanical twining of the magnesium matrix observed in Fig. 6 is caused by the relaxation of the matrix and is directly connected to high residual stresses. On the other hand, the SPS sample exhibited a fully recrystallised microstructure with equiaxed grains. A comparable microstructure was repeatedly reported for similarly processed magnesium alloys [18,19]. The temperature profile has a major impact on the final microstructure, and in our case, a relatively high temperature was selected to stimulate the aforementioned enhanced interconnection of the powder particles by disruption of the oxide layer. Nevertheless, while the impact of temperature on the residual strain is strong [19,50], its effect on the average grain size is rather low [18,31].

The crystallographic texture of both SLM and SPS samples was strongly related to the individual processing methods. The dominant texture component in the SLM sample, with the strength of ∼5 times random, was {11–20}<10–10> oriented almost parallel to the Z direction. There are only several reports discussing the origin of the crystallographic texture which forms during SLM, and it is commonly associated with preferential growth of the dendrites from the melt pool [51,52]. The most favourable growth direction during SLM is close to the Z-direction and declines towards the laser motion direction with magnitude depending on the laser power density [51]. The preferred growth direction of magnesium dendrites in binary alloys is almost always <11–20> [53], and the measured texture shown in Fig. 7 corresponds to such an explanation. The limited number of reports presenting texture formed in the SLM-prepared magnesium alloys showed either weak/random texture [46,48] or {0001} basal texture in the Z-direction [30,47,54]. However, these studies also reported highly recrystallised grain structures and alloys that contained a much higher amount of the alloying elements. Finally, the texture formation during SLM may be dependent on composition and processing parameters. Regarding the SPS sample, a very weak {0001} basal texture was measured with a strength of only ∼2 times random. Formation of this component, which is parallel to the SLD direction, resulted from random crystalline orientation prior to the sintering and application of external load in the SLD direction. Partial deformation and reorientation of a small fraction of grains with basal planes perpendicular to the external load subsequently contributed to the formation of the {0001} basal texture component. Comparable texture formation was observed already in the WN43 alloy processed similarly [12]. The typical weak "rare-earth" texture, with a strength of ∼2 times random, was formed in the extruded sample, which is comparable to the previous results [22].

4.2. Mechanical properties

Even though the microstructure differences between the investigated materials were rather significant, the onset of the plastic deformation (yield strength) and microhardness were comparable between the materials and the deformation modes. The mechanical properties of the investigated materials are closely related to the microstructure. The factors originating in grain boundaries, secondary phases (size and distribution), residual strain, solid solution elements and texture have a strong impact on the resulting strength. From the microstructural point of view, the dominant strengthening factor for the SLM sample was the fine distribution of precipitates and high residual strain. Even though the SLM samples comprised relatively large grains, a high fraction of twin boundaries contributed to the material strength as well. In the case of the SPS sample, grain boundaries (it featured the smallest grain size) and precipitates inside the former powder boundaries have the dominant effect on strength. Finally, the grain boundaries and dissolved Y in the magnesium matrix had a major impact on strength in the case of the EX sample. The SPS and EX samples exhibited a weak crystallographic texture, therefore, it did not have a severe impact on the yield stress and only insignificant yield stress asymmetry was measured, as evidenced by only a negligible difference between the respective CYS and TYS values. Mechanical twinning was more pronounced in the extruded sample (sigmoidal shape in compression), likely because of larger grain size and lack of precipitates, which hinder the formation and growth of twins [55]. The texture in the SLM sample was much stronger, but the basal component in the (0001) pole figure was in the "hard" orientation for both measured deformation modes (X-direction) and thus did not lead to any yield point asymmetry. Nevertheless, this kind of texture may have a strong strengthening effect for both deformation modes, which needs to be considered as well [56], and potentially causes spatial asymmetry (not measured here) of the mechanical properties of the SLM material.

The notable difference in the deformability between the SLM and SPS samples arises primarily from the residual porosity (∼0.3% vs. negligible for the SLM and SPS materials, respectively), as well as the residual stresses (present only in the SLM material) and grain structure (inhomogeneous in the case of the SLM material). A combined effect of these microstructural features explains (i) the relatively low fracture strain of the SLM sample and (ii) the DIC results that showed that the SPS samples deformed uniformly up to ∼15% of plastic deformation, while strain localisation was detected already after ∼1% of plastic deformation in the case of the SLM sample, cf. Fig. 9. The cracks are expected to be more prone to initialise at the pores and/or in the vicinity of the highly strained areas present in the SLM material. Subsequently, crack propagation along such weak spots and the grain boundaries (especially of large grains oriented perpendicular to the load direction) is promoted and causes brittle fracture, as observed in Fig. 10. On the other hand, the SPS sample did not suffer from any of these attributes, and together with the aforementioned very good interconnection of the individual powder particles, exceptional deformability in tension was measured for this material, compared to other SPS-prepared magnesium alloys [12,57].

The mechanical strength of the SLM-prepared magnesium alloys differs substantially depending on the composition and processing parameters. Usually, a higher microhardness (up to 120 HV) and yield strength (up to 300 MPa) were reported for Mg alloys. However, as mentioned above, heavily al-

loyed systems often exhibit a more recrystallised grain structure with a smaller grain size and benefit from a significant contribution of secondary particle strengthening [10,16,58,59]. Some of these alloys exhibited comparable deformability and higher strength than the W3 alloy investigated in this study [42,46,47]. On the other hand, low-alloyed magnesium alloys or pure Mg exhibited higher strength only together with very low deformability because the selected processing parameters resulted in finer microstructure and higher porosity [60]. The yield strength (in both directions) of the SPS-prepared W3 alloy (∼110 MPa) was found to be lower than the one of the WN43 alloy (∼150 MPa) investigated in our previous study, but the deformability significantly increased (∼13% vs. ∼21%) [12]. Considering other reports, highly alloyed magnesium alloys (e.g., AZ91, AZ80, WE43) were repeatedly prepared by SPS, leading to much higher strength (microhardness up to 91 HV, yield strength up to 330 MPa) but significantly lower deformability [57,61–65]. To the authors' knowledge, the here-reported deformability in tension is the highest for magnesium alloy prepared by SPS.

In general, this work unambiguously showed that the powder metallurgy techniques might be a good option for the preparation of the biodegradable W3 magnesium alloy. The mechanical strength is comparable between SLM/SPS and conventional extrusion. Moreover, the SPS-prepared material also features excellent deformability unrivalled within the class of Mg alloys prepared by powder metallurgy.

4.3. Corrosion resistance

The linear polarisation method revealed that there is only a minor difference in the susceptibility to corrosion in the early stage of degradation (10 min) between the investigated materials. From the thermodynamic point of view, the extruded material showed slightly nobler corrosion potential than the samples prepared via powder metallurgy. This is due to the higher amount of yttrium dissolved in the magnesium matrix, unlike in the other two materials [5]. On the other hand, from the kinetic point of view, the lowest corrosion rate was measured for the SLM sample. This result seems to contradict the immersion test results, which showed that the SLM sample corroded the fastest, whereas the degradation rate of the other two materials was the same within the error. This discrepancy can be explained by the microstructure differences in the material. The SLM sample had a relatively high residual strain, which increases the propensity for faster degradation [66]. Therefore, more rapid formation of the corrosion products' surface film (within 10 min of immersion) resulted in a decreased corrosion rate measured by the polarisation resistance. A comparable effect was repeatedly measured in some ultrafine-grain magnesium alloys with lower degradation rates than their coarse-grain counterparts despite the higher surface density of lattice defects [67,68].

Further, the fast degradation of the SLM sample during the immersion test may be related to the combination of large and deformed grains, porosity, and depletion of yttrium from the magnesium matrix at the expense of the shattered magnesium oxides. A minor negative effect of the $Mg_{24}Y_5$ phase particles (galvanic micro-cell) is expected, but the overall volume fraction of this phase was very low. Unlike ultrafine-grain materials, the initial fast formation of the protective surface layer did not provide long-term protection. Because of high residual strain and large grains, the surface layer was prone to cracking and detachment of large fragments, as shown in Fig. 12. The observed residual porosity also promotes corrosion penetration into the material [31]. On the other hand, the SPS and EX samples exhibited a similar corrosion rate after 7 days of immersion despite the predominant concentration of yttrium along the former powder boundaries in the case of the SPS sample. Both SPS and EX materials had comparable grain sizes and low residual strain. The depletion of yttrium from the SPS sample magnesium matrix was compensated for by the formation of yttrium-rich former powder boundaries, which appeared to be very effective in hindering the corrosion front propagation (Fig. 12). A similar result was also reported for the WN43 alloy prepared by SPS [31]. Overall, the SPS method was found to be very effective for preparing the biodegradable W3 alloy from the degradation point of view, while more thorough microstructure tailoring is needed for the SLM-prepared material. Comparable degradation properties between the SPS-prepared and extruded materials is a highly auspicious result, considering the previously reported exceptional *in vitro* degradation performance of the extruded W3 alloy [9].

5. Conclusions

A biodegradable magnesium alloy Mg-3Y (W3) was prepared by two powder metallurgy techniques – selective laser melting (SLM) and spark plasma sintering (SPS), and the microstructure, mechanical properties and corrosion resistance were thoroughly characterised. The results were compared to the conventionally extruded counterpart. The following results may be drawn from this study:

- Successful consolidation of the metallic powder resulted in no residual porosity in the case of the SPS material and very low porosity of <0.3% for the SLM material.
- The dominant secondary phase found in both SLM and SPS samples was Y_2O_3, which had already formed on the surface of the initial powder particles. Its distribution was, however, significantly affected by the consolidation process.
- A fine-grained recrystallised microstructure was achieved by SPS, while large, strained grains containing a high amount of deformation twins were observed in the SLM sample.
- The mechanical strength was comparable for all three investigated materials. The SPS sample exhibited extraordinary plastic deformability in tension of ∼21%. On the other hand, deformability of only ∼9% was measured for the SLM sample because of strain localisation.
- The corrosion resistance measurements revealed that the degradation rate of the SPS sample was similar to the

extruded counterpart. On the contrary, the SLM sample showed severe degradation because of the combination of large, strained grains and residual porosity.
- The major outcome of this study is that the SPS consolidation method is very effective in the preparation of the W3 biodegradable alloy, resulting in a material with convenient mechanical and degradation properties that might find practical applications.

Declaration of competing interest

Peter Minarik is an editorial board member for the Journal of Magnesium and Alloys and was not involved in the editorial review or the decision to publish this article. All authors declare that there are no competing interests.

CRediT authorship contribution statement

P. Minárik: Writing – original draft, Visualization, Methodology, Formal analysis, Conceptualization. **M. Zemková:** Investigation, Conceptualization, Writing – original draft. **S. Šašek:** Investigation, Visualization. **J. Dittrich:** Investigation. **M. Knapek:** Formal analysis, Investigation, Methodology. **F. Lukáč:** Investigation, Resources. **D. Koutný:** Resources. **J. Jaroš:** Resources. **R. Král:** Conceptualization, Methodology.

Acknowledgement

This work was supported by the Czech Science Foundation under project no. 22-21122J. Partial financial support from the Ministry of Health of the Czech Republic under the grant Nr. 20-08-00150 is acknowledged. M.Z. acknowledges partial financial support from the Charles University Grant Agency under project number 389422. P. M. acknowledges partial financial support from the Science Grant Agency of the Slovak Republic through project No. 1/0153/21. D. K. and J. J. would like to thank faculty specific research project FSI-S-23-8340.

References

[1] V. Tsakiris, C. Tardei, F.M. Clicinschi, J. Magnes. Alloys 9 (2021) 1884–1905, doi:10.1016/j.jma.2021.06.024.
[2] J. Liu, D. Bian, Y. Zheng, X. Chu, Y. Lin, M. Wang, Z. Lin, M. Li, Y. Zhang, S. Guan, Acta Biomater. 102 (2020) 508–528, doi:10.1016/j.actbio.2019.11.013.
[3] Y. Dai, Y. Tang, X. Xu, Z. Luo, Y. Zhang, Z. Li, Z. Lin, S. Zhao, M. Zeng, B. Sun, L. Cheng, J. Zhu, Z. Xiong, H. Long, Y. Zhu, K. Yu, J. Biomed. Mater. Res. B Appl. Biomater. 107 (2019) 2537–2548, doi:10.1002/jbm.b.34344.
[4] P. Lovašiová, T. Lovaši, J. Kubásek, E. Jablonská, Š. Msallamová, A. Michalcová, D. Vojtěch, J. Suchý, D. Koutný, E. Ghassan Hamed Alzubi, Metals 12 (2022) 469, doi:10.3390/met12030469.
[5] X. Liu, D. Shan, Y. Song, E. Han, J. Magnes. Alloys 5 (2017) 26–34, doi:10.1016/j.jma.2016.12.002.
[6] H.T. Son, J.S. Lee, C.S. Kang, J.C. Bae, K. Yoshimi, K. Maruyama, Mater. Trans. 49 (2008) 945–951, doi:10.2320/matertrans.MC200777.
[7] A.J. Davenport, C. Padovani, B.J. Connolly, N.P.C. Stevens, T.A.W. Beale, A. Groso, M. Stampanoni, Electrochem. Solid-State Lett. 10 (2006) C5, doi:10.1149/1.2400727.
[8] A.D. Sudholz, K. Gusieva, X.B. Chen, B.C. Muddle, M.A. Gibson, N. Birbilis, Corros. Sci. 53 (2011) 2277–2282, doi:10.1016/j.corsci.2011.03.010.
[9] M. Zemková, P. Minárik, E. Jablonská, J. Veselý, J. Bohlen, J. Kubásek, J. Lipov, T. Ruml, V. Havlas, R. Král, Materials 15 (2022) 7571, doi:10.3390/ma15217571.
[10] M. Ahmadi, S.A.A.B. Tabary, D. Rahmatabadi, M.S. Ebrahimi, K. Abrinia, R. Hashemi, J. Mater. Res. Technol. 19 (2022) 1537–1562, doi:10.1016/j.jmrt.2022.05.102.
[11] N. Sezer, Z. Evis, S.M. Kayhan, A. Tahmasebifar, M. Koç, J. Magnes. Alloys 6 (2018) 23–43, doi:10.1016/j.jma.2018.02.003.
[12] M. Knapek, P. Minárik, A. Greš, M. Zemková, F. Lukáč, J. Bohlen, F. Chmelík, R. Král, Mater. Sci. Eng. A 849 (2022) 143481, doi:10.1016/j.msea.2022.143481.
[13] P. Cavaliere, Spark Plasma Sintering of Materials: Advances in Processing and Applications, Springer International Publishing, Cham, 2019, doi:10.1007/978-3-030-05327-7.
[14] S. Dasgupta, Y.P. Singh, in: Advanced Additive Manufacturing, Elsevier, 2023, pp. 103–127, doi:10.1016/B978-0-323-91834-3.00009-0.
[15] W.N. Zhang, L.Z. Wang, Z.X. Feng, Y.M. Chen, Optik 207 (2020), doi:10.1016/j.ijleo.2019.163842.
[16] Y. Zhou, K. Zhang, Y. Liang, J. Cheng, Y. Dai, Materials 15 (2022) 7049, doi:10.3390/ma15207049.
[17] H.T. Son, J.M. Hong, I.H. Oh, J.S. Lee, T.S. Kim, K. Maruyama, Solid State Phenom. 124–126 (2007) 1517–1520, doi:10.4028/www.scientific.net/SSP.124-126.1517.
[18] P. Minárik, J. Stráský, J. Veselý, F. Lukáč, B. Hadzima, R. Král, J. Alloys Compd. 742 (2018) 172–179, doi:10.1016/j.jallcom.2018.01.115.
[19] P. Minárik, M. Zemková, F. Lukáč, J. Bohlen, M. Knapek, R. Král, J. Alloys Compd. 819 (2020) 153008, doi:10.1016/j.jallcom.2019.153008.
[20] P. Minárik, M. Zemková, J. Veselý, F. Lukáč, J. Bohlen, M. Knapek, R. Král, Mater. Lett. 292 (2021) 129647, doi:10.1016/j.matlet.2021.129647.
[21] J. Blaber, B. Adair, A. Antoniou, Exp. Mech. 55 (2015) 1105–1122, doi:10.1007/s11340-015-0009-1.
[22] P. Minárik, D. Drozdenko, M. Zemková, J. Veselý, J. Čapek, J. Bohlen, P. Dobroň, Mater. Sci. Eng. A 759 (2019) 455–464, doi:10.1016/j.msea.2019.05.069.
[23] Y.R. Zhao, L.L. Chang, J. Guo, Y.P. Jin, J. Magnes. Alloys 7 (2019) 90–97, doi:10.1016/j.jma.2018.12.004.
[24] M.R. Barnett, Mater. Sci. Eng. A 464 (2007) 1–7, doi:10.1016/j.msea.2006.12.037.
[25] K.E. Prasad, B. Li, N. Dixit, M. Shaffer, S.N. Mathaudhu, K.T. Ramesh, JOM 66 (2014) 291–304, doi:10.1007/s11837-013-0850-6.
[26] P. Minárik, F. Lukáč, J. Cinert, S. Šašek, R. Král, in: Proceedings of the 27th International Conference on Metallurgy and Materials, Metal 2018, 2018, pp. 1401–1406.
[27] W.N.A.W. Muhammad, Z. Sajuri, Y. Mutoh, Y. Miyashita, J. Alloys Compd. 509 (2011) 6021–6029, doi:10.1016/j.jallcom.2011.02.153.
[28] J. Kubásek, P. Minárik, K. Hosová, S. Šašek, M. Knapek, J. Veselý, J. Stráská, D. Dvorský, M. Čavojský, D. Vojtěch, J. Alloys Compd. 877 (2021) 160089, doi:10.1016/j.jallcom.2021.160089.
[29] W. Wang, L. He, X. Yang, D. Wang, J. Alloys Compd. 868 (2021) 159107, doi:10.1016/j.jallcom.2021.159107.
[30] F. Bär, L. Berger, L. Jauer, G. Kurtuldu, R. Schäublin, J.H. Schleifenbaum, J.F. Löffler, Acta Biomater. 98 (2019) 36–49, doi:10.1016/j.actbio.2019.05.056.
[31] M. Knapek, M. Zemková, A. Greš, E. Jablonská, F. Lukáč, R. Král, J. Bohlen, P. Minárik, J. Magnes. Alloys (2021), doi:10.1016/j.jma.2020.12.017.
[32] T.B. Massalski, H. Okamoto, Binary Alloy Phase Diagrams, 2nd ed., The Materials Information Society, Ohio, 1990 Materials Park.
[33] Y. Huang, L. Yang, S. You, W. Gan, K.U. Kainer, N. Hort, J. Magnes. Alloys 4 (2016) 173–180, doi:10.1016/j.jma.2016.08.002.
[34] M. Vlček, J. Čížek, F. Lukáč, P. Hruška, B. Smola, I. Stulíková, H. Kudrnová, P. Minárik, T. Kmječ, T. Vlasák, Int. J. Hydrog. Energy 42 (2017) 22598–22604, doi:10.1016/j.ijhydene.2017.04.012.

[35] C. He, S. Bin, P. Wu, C. Gao, P. Feng, Y. Yang, L. Liu, Y. Zhou, M. Zhao, S. Yang, C. Shuai, Metals 7 (2017) 105, doi:10.3390/met7030105.
[36] B. Zhang, H. Liao, C. Coddet, Mater. Des. 34 (2012) 753–758, doi:10.1016/j.matdes.2011.06.061.
[37] C.C. Ng, M.M. Savalani, M.L. Lau, H.C. Man, Appl. Surf. Sci. 257 (2011) 7447–7454, doi:10.1016/j.apsusc.2011.03.004.
[38] D. Hu, Y. Wang, D. Zhang, L. Hao, J. Jiang, Z. Li, Y. Chen, Mater. Manuf. Process. 30 (2015) 1298–1304, doi:10.1080/10426914.2015.1025963.
[39] C. Liu, M. Zhang, C. Chen, Mater. Sci. Eng. A 703 (2017) 359–371, doi:10.1016/j.msea.2017.07.031.
[40] X. Wang, C. Chen, M. Zhang, Rapid Prototyp. J. 26 (2020) 841–854, doi:10.1108/RPJ-04-2019-0113.
[41] S. Liu, H. Guo, Mater. Lett. 265 (2020) 127463, doi:10.1016/j.matlet.2020.127463.
[42] N.A. Zumdick, L. Jauer, L.C. Kersting, T.N. Kutz, J.H. Schleifenbaum, D. Zander, Mater. Charact. 147 (2019) 384–397, doi:10.1016/j.matchar.2018.11.011.
[43] C. Shuai, L. Liu, M. Zhao, P. Feng, Y. Yang, W. Guo, C. Gao, F. Yuan, J. Mater. Sci. Technol. 34 (2018) 1944–1952, doi:10.1016/j.jmst.2018.02.006.
[44] C. Gao, S. Li, L. Liu, S. Bin, Y. Yang, S. Peng, C. Shuai, J. Magnes. Alloys 9 (2021) 305–316, doi:10.1016/j.jma.2020.03.016.
[45] G.T. Gray, V. Livescu, P.A. Rigg, C.P. Trujillo, C.M. Cady, S.R. Chen, J.S. Carpenter, T.J. Lienert, S.J. Fensin, Acta Mater. 138 (2017) 140–149, doi:10.1016/j.actamat.2017.07.045.
[46] X. Li, X. Fang, S. Wang, S. Wang, M. Zha, K. Huang, J. Magnes. Alloys (2022), doi:10.1016/j.jma.2022.06.004.
[47] Q. Deng, Y. Zhang, Z. Liu, Z. Chang, N. Su, Y. Wu, L. Hao, L. Peng, W. Ding, J. Alloys Compd. 910 (2022) 164863, doi:10.1016/j.jallcom.2022.164863.
[48] P. Fu, N. Wang, H. Liao, W. Xu, L. Peng, J. Chen, G. Hu, W. Ding, Trans. Nonferr. Met. Soc. China 31 (2021) 1969–1978, doi:10.1016/S1003-6326(21)65630-3.
[49] S. Waqar, K. Guo, J. Sun, Opt. Laser Technol. 149 (2022) 107806, doi:10.1016/j.optlastec.2021.107806.
[50] P. Angerer, J. Wosik, E. Neubauer, L.G. Yu, G.E. Nauer, K.A. Khor, Int. J. Refract. Met. Hard Mater. 27 (2009) 105–110, doi:10.1016/j.ijrmhm.2008.04.002.
[51] Y. Wang, J. Shi, Mater. Charact. 165 (2020) 110372, doi:10.1016/j.matchar.2020.110372.
[52] S.D. Jadhav, S. Dadbakhsh, L. Goossens, J.P. Kruth, J. Van Humbeeck, K. Vanmeensel, J. Mater. Process. Technol. 270 (2019) 47–58, doi:10.1016/j.jmatprotec.2019.02.022.
[53] J. Du, Z. Guo, A. Zhang, M. Yang, M. Li, S. Xiong, Sci. Rep. 7 (2017) 13600, doi:10.1038/s41598-017-12814-5.
[54] Q. Deng, Y. Wu, Q. Wu, Y. Xue, Y. Zhang, L. Peng, W. Ding, Addit. Manuf. 49 (2022) 102517, doi:10.1016/j.addma.2021.102517.
[55] C. Liu, P. Shanthraj, J.D. Robson, M. Diehl, S. Dong, J. Dong, W. Ding, D. Raabe, Acta Mater. 178 (2019) 146–162, doi:10.1016/j.actamat.2019.07.046.
[56] J. Dittrich, G. Farkas, D. Drozdenko, M. Knapek, K. Máthis, P. Minárik, J. Alloys Compd. 937 (2023) 168388, doi:10.1016/j.jallcom.2022.168388.
[57] D. Dvorsky, J. Kubasek, E. Jablonska, J. Kaufmanova, D. Vojtech, J. Alloys Compd. 825 (2020) 154016, doi:10.1016/j.jallcom.2020.154016.
[58] Y. Zhou, P. Wu, Y. Yang, D. Gao, P. Feng, C. Gao, H. Wu, Y. Liu, H. Bian, C. Shuai, J. Alloys Compd. 687 (2016) 109–114, doi:10.1016/j.jallcom.2016.06.068.
[59] C. Chang, H. Liao, L. Yi, Y. Dai, S.C. Cox, M. Yan, M. Liu, X. Yan, Adv. Powder Mater. 2 (2023) 100097, doi:10.1016/j.apmate.2022.100097.
[60] L. Peng, Q. Deng, Y. Wu, P. Fu, Z. Liu, Q. Wu, K. Cheng, Acta Met. Sin. 59 (2022) 31–54, doi:10.11900/0412.1961.2022.00166.
[61] B. Zheng, O. Ertorer, Y. Li, Y. Zhou, S.N. Mathaudhu, C.Y.A. Tsao, E.J. Lavernia, Mater. Sci. Eng. A 528 (2011) 2180–2191, doi:10.1016/j.msea.2010.11.073.
[62] M. Mondet, E. Barraud, S. Lemonnier, J. Guyon, N. Allain, T. Grosdidier, Acta Mater. 119 (2016) 55–67, doi:10.1016/j.actamat.2016.08.006.
[63] J. Soderlind, M. Cihova, R. Schäublin, S. Risbud, J.F. Löffler, Acta Biomater. 15 (2019) 67–80, doi:10.1016/j.actbio.2019.06.045.
[64] K.R. Kim, H.S. Kim, S.H. Kwon, D.Y. Hwang, J. Korean Phys. Soc. 65 (2014) 1669–1674, doi:10.3938/jkps.65.1669.
[65] M. Mondet, E. Barraud, S. Lemonnier, N. Allain, T. Grosdidier, J. Alloys Compd. 698 (2017) 259–266, doi:10.1016/j.jallcom.2016.12.066.
[66] I.J. Son, H. Nakano, S. Oue, S. Kobayashi, H. Fukushima, Z. Horita, Mater. Trans. 49 (2008) 2656–2663, doi:10.2320/matertrans.MRA2008230.
[67] P. Minárik, R. Král, M. Janeček, Appl. Surf. Sci. 281 (2013) 44–48, doi:10.1016/j.apsusc.2012.12.096.
[68] P. Minárik, E. Jablonská, R. Král, J. Lipov, T. Ruml, C. Blawert, B. Hadzima, F. Chmelík, Mater. Sci. Eng. C 73 (2017) 736–742, doi:10.1016/j.msec.2016.12.120.